

Article

Effect of X-Ray Tube Configuration on Measurement of Key Soil Fertility Attributes with XRF

Tiago Rodrigues Tavares ^{1,2}, José Paulo Molin ^{1,*}, Lidiane Cristina Nunes ³,
Elton Eduardo Novais Alves ⁴, Fábio L. Melquiades ⁵,
Hudson Wallace Pereira de Carvalho ⁶ and Abdul Mounem Mouazen ²

¹ Laboratory of Precision Agriculture (LAP), Department of Biosystems Engineering, “Luiz de Queiroz” College of Agriculture (ESALQ), University of São Paulo (USP), Piracicaba, São Paulo 13418900, Brazil; tiagosrt@usp.br

² Precision Soil and Crop Engineering Group (Precision SCoRing), Department of Environment, Faculty of Bioscience Engineering, Ghent University, Coupure Links 653, Blok B, 1st Floor 9000 Gent, Belgium; abdul.mouazen@ugent.be

³ Laboratory of Analytical Chemistry (LQA), Center for Nuclear Energy in Agriculture (CENA), University of São Paulo (USP), Piracicaba, São Paulo 13416000, Brazil; lcnunes@cena.usp.br

⁴ Laboratory of 14 Carbon (LC14), Center for Nuclear Energy in Agriculture (CENA), University of São Paulo (USP), Piracicaba, São Paulo 13416000, Brazil; elton.alves@usp.br

⁵ Laboratory of Applied Nuclear Physics (LFNA), Department of Physics, Londrina State University (UEL), Londrina, Paraná 86057970, Brazil; fmelquiades@uel.br

⁶ Laboratory of Nuclear Instrumentation (LIN), Center for Nuclear Energy in Agriculture (CENA), University of São Paulo (USP), Piracicaba, São Paulo 13416000, Brazil; hudson@cena.usp.br

* Correspondence: jpmolin@usp.br; Tel.: +55-19-3447-8502

Received: 14 February 2020; Accepted: 13 March 2020; Published: 17 March 2020



Abstract: The successful use of energy-dispersive X-ray fluorescence (ED-XRF) sensors for soil analysis requires the selection of an optimal procedure of data acquisition and a simple modelling approach. This work aimed at assessing the performance of a portable XRF (XRF) sensor set up with two different X-ray tube configurations (combinations of voltage and current) to predict nine key soil fertility attributes: clay, organic matter (OM), cation exchange capacity (CEC), pH, base saturation (V), and extractable nutrients (P, K, Ca, and Mg). An XRF, operated at a voltage of 15 kV (and current of 23 μ A) and 35 kV (and current of 7 μ A), was used for analyzing 102 soil samples collected from two agricultural fields in Brazil. Two different XRF data analysis scenarios were used to build the predictive models: (i) 10 emission lines of 15 keV spectra (EL-15), and (ii) 12 emission lines of 35 keV spectra (EL-35). Multiple linear regressions (MLR) were used for model calibration, and the models' prediction performance was evaluated using different figures of merit. The results show that although X-ray tube configuration affected the intensity of the emission lines of the different elements detected, it did not influence the prediction accuracy of the studied key fertility attributes, suggesting that both X-ray tube configurations tested can be used for future analyses. Satisfactory predictions with residual prediction deviation (RPD) ≥ 1.54 and coefficient of determination (R^2) ≥ 0.61 were obtained for eight out of the ten studied soil fertility attributes (clay, OM, CEC, V, and extractable K, Ca, and Mg). In addition, simple MLR models with a limited number of emission lines was effective for practical soil analysis of the key soil fertility attributes (except pH and extractable P) using XRF. The simple and transparent methodology suggested also enables future researches that seek to optimize the XRF scanning time in order to speed up the XRF analysis in soil samples.

Keywords: precision agriculture; proximal soil sensing; hybrid laboratory; soil testing; XRF spectroscopy; Brazilian tropical soils

1. Introduction

Precision agriculture (PA) approaches that seek to optimize the use of fertilizers have great potential to boost agronomic and environmental benefits in agricultural production systems [1]. This requires a detailed characterization of soil fertility in the field, which is fundamental to the implementation of variable rate fertilization. However, reliable characterizations of within-field spatial variability in soil fertility requires high sampling density, which comes at high costs related to sample acquisition and traditional soil testing in commercial laboratories [2]. Proximal soil sensing (PSS) is considered as an alternative approach to analyse soil in a practical and environmentally friendly way that allows an increase in sampling density without relying exclusively on traditional soil tests [3–5].

Sensors compatible with PSS approaches can be applied in laboratory and field conditions, and some of them can be used for on-line measurements, assembled on mobile platforms [1]. In order to create practical alternatives for soil analysis, efforts have been made worldwide to adapt and re-engineer sensor systems developed in other areas into soil sensing [6,7], as well as assessing different combinations of sensors and data fusion methods [8–10]. However, there is still no consensus on an effective technique that enables the development of a generic and robust methodology for soil fertility analysis via proximal sensors. The development of a hybrid methodology suitable for laboratory and field applications for the prediction of soil fertility attributes should play an important role in soil analysis, as commented by Molin and Tavares [1].

X-ray fluorescence (XRF) spectrometry is one of the promising PSS techniques, as it allows analyses with satisfactory performance using minimum sample preparation [11]. Its recent popularization has made it attractive for joint implementation with other popular techniques, such as visible and near infrared spectroscopy (visNIRS) [8,9]. XRF sensors enable measuring the total content of specific elements in the soil (e.g., Fe, Al, Si, Ca, and K) and can be used as a proxy for indirect predictions of other soil attributes (e.g., pH, cation exchange capacity (CEC) and texture) [12]. Some researchers have applied XRF sensors to assess fertility attributes in soil samples and satisfactory results were reported for soil texture [13], pH [14], CEC [15], base saturation (V) [16], total content of nutrients [17], and extractable nutrients [18]. In Brazilian tropical soils, recent research has shown promising performance for organic matter (OM) [19], extractable nutrients (K, Ca, and Mg) [20,21], chemical attributes (e.g., CEC, V, and pH) [20,22,23], and texture [24]. Studies applying XRF in agricultural soils for predicting key fertility attributes are still preliminary and further works are needed for a comprehensive understanding of its applications particularly in tropical soils [21,25].

Most of the studies that applied XRF in the PSS context used pre-developed (pre-programmed) measurement packages (e.g., Soil Mode, Innov-X Systems, Inc., MA, USA), which have specific routines for spectra acquisition and processing [13–15,20–22,25–27]. These routines involve the standardization of some parameters, such as (i) X-ray tube configurations (e.g., voltage and current), (ii) number consecutive irradiations, (iii) scanning time (dwell time), (iv) filters and (v) types of spectral pre-processing (e.g., Compton normalization, etc). Although these packages allow for a user-friendly approach that contributes to the popularization and expansion of the XRF application, they are not fully transparent and do not allow for flexibility regarding the time of analysis. Faster XRF analyses are fundamental to increase the agility of benchtop analysis, as well as creating new perspective for using this sensor embedded on mobile sensor platforms for on-line measurements. Therefore, the development of clear and objective methods of operating XRF should be prioritized [28], since they allow for an unbiased scientific evaluation and also the optimization of data acquisition and processing routines necessary to reduce the time of analysis with XRF sensors.

The X-ray tube voltage and current are important configurations of the energy-dispersive X-ray fluorescence (ED-XRF) equipment. ED-XRF equipment uses a polychromatic beam (also called continuous radiation or *bremstrahlung* radiation) to excite the sample and, by changing the voltage of the tube, the energy intensity and the amplitude of this continuous spectrum are changed [29]. In turn, as the current is increased, the X-ray intensity (number of photons emitted from the tube filament, e.g., the photon flux) of the continuous spectrum also increases [30]. In other words, the voltage impacts the energy range and intensity of the continuous spectrum used for excitation while current impacts mostly its intensity.

Hence, the X-ray tube configuration alters the fluorescence yield of a given analyte [31] and can, therefore, impact the performance of prediction models. Usually, lower voltages of the X-ray tube (≤ 15 keV) increase the fluorescence yield of light elements (e.g., Si, Al, K, Ca, etc.), which can be a promising setup in XRF analyses of agricultural soils. On the other hand, a spectrum acquired at such low voltage does not contain the well-defined $K\alpha$ scattering peaks, which are usually present when using higher energies. For example, in equipment with Rh-anode tube, the elastic (Thomson) and inelastic (Compton) scattering peaks appear between 18 and 22 keV. However, these scattered X-rays can also be important because they can be explored as a source of soil information [32]. The intensity of the XRF scattering energy is inversely related to the average atomic number of the sample, which can allow inferring about soil density and its related attributes (e.g., OM and texture). An innovative study conducted by Morona et al. [19] in Brazilian soils showed a good relationship between the XRF scattering region and OM contents.

Since most of the works that have evaluated XRF sensors in the PSS context used pre-developed measurement packages, the influence of X-ray tube configuration on fertility attribute predictions has not yet been addressed in the literature. Given the need to understand the effect of the X-ray tube configuration to establish practical and transparent methodologies for XRF data acquisition, this work aimed to evaluate the performance of a portable ED-XRF configured with different X-ray tube voltages (15 and 35 kV) to predict key fertility attributes in agricultural fields under tropical environment.

2. Materials and Methods

2.1. Study Sites and Soil Samples

The samples used in this study belong to the soil sample bank of the Precision Agriculture Laboratory (LAP) from Luiz de Queiroz College of Agriculture, University of São Paulo. They were collected from 0–20 cm depth and stored after being air-dried, ground and sieved (≤ 2 mm). The samples used in this work are from two different fields (Figure 1) that have been under active agricultural production over the years. Field 1 is located in the southeast region of Brazil, in the municipality of Piracicaba, State of São Paulo. Its soil is classified as Lixisol [33] with a clayey texture and high nutrient variability. Field 2 is situated in Brazil's midwest region, in the municipality of Campo Novo do Parecis, State of Mato Grosso. Its soil is classified as Ferralsol [33], with a texture varying between sandy loam and sandy clay loam. A set of 102 soil samples were selected for this work—58 soil samples from Field 1 and 44 from Field 2. The chemical analysis results of the LAP's soil sample bank were used to choose samples with wide ranges of variability of key fertility attributes in both study fields. After dataset selection, the samples were again subjected to laboratory chemical analyses, as described in Section 2.2, which provided the results of the reference analyses used in this work.

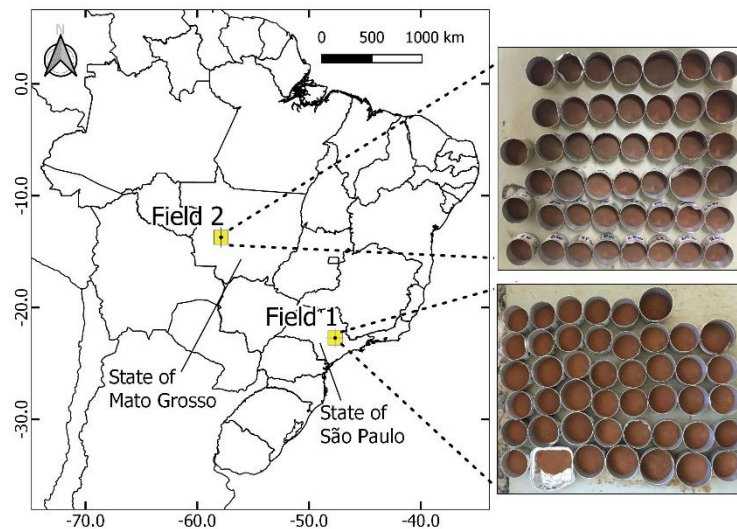


Figure 1. Location of Field 1 and Field 2 in Brazil, where the soil samples were collected.

2.2. Reference Analyses

From each sample, an aliquot of 90 g was sent to the laboratory for regular soil fertility analysis. These analyses determined clay, OM, CEC, pH, V, and extractable nutrients (P, K, Ca, and Mg), following the methods described by Van Raij et al. [34]. Clay content was quantified by the Bouyoucos hydrometer method in a dispersing solution. OM concentration was determined via oxidation with potassium dichromate solution. pH was determined via calcium chloride solution. Extractable nutrients were determined via ion exchange resin extraction, being designated in this work as resin-extracted (re-) P and exchangeable (ex-) K, Ca, and Mg. The soil potential acidity (H + Al) was quantified via pH in buffer solution method (SMP) and used to calculate the CEC, which corresponds to the sum of soil potential acidity and sum of bases (ex-Ca + ex-Mg + ex-K). Percent base saturation (V) was calculated by the ratio between the sum of bases and CEC.

The pseudo total content (ptc) of P, K, Ca, and Mg was also analysed following the United States Environmental Protection Agency (USEPA) Method 3051A [35]. This method comprises the chemical dissolution of pulverized soil samples using HNO₃ and HCl, with microwave-assisted digestion. Then, the multi-element quantification is performed using inductively coupled plasma optical emission spectrometry (ICP - OES). For the determination of elements in tropical soils, this method presents proportional recoveries compared to more aggressive methods (e.g., EPA 3052, which uses HF) [36], thus allowing us to understand the relationship between the total and extractable contents of the elements of interest. Linear correlations were performed between the extractable and pseudo total content of P, K, Ca, and Mg. A correlation matrix was calculated among fertility attributes to better understand their interrelations.

2.3. pXRF Measurements with Different Settings

Soil samples were scanned after being air-dried and sieved at 2 mm, as suggested by Tavares et al. [11]. Ten grams of each sample was placed in an XRF polyethylene cup of 31 mm diameter (n. 1530, Chemplex Industries Inc., USA) sealed at the bottom with a 4- μ m thick polypropylene film (n. 3520, SPEX, USA). Each sample was scanned in triplicate and the sample cup was repositioned between scans. The replicates were subsequently averaged for analysis.

XRF spectra were acquired using a Tracer III-SD model (Bruker AXS, Madison, EUA). This hand-held instrument is equipped with a 4 W Rh X-ray tube and an X-Flash[®] Peltier-cooled Silicon Drift Detector (Bruker AXS, Madison, USA). This detector has 2048 channels and an active area of 10 mm². All samples were scanned using the XRF sensor, configured with two tube voltage conditions: 15 and 35 kV. For each voltage, the current was set so as not to exceed 15% of the detector deadtime,

avoiding spectral distortions and artefacts; thus, the tube current was set at 23 and 7 μA for the voltages of 15 and 35 kV, respectively. These conditions correspond to a tube working power of 0.245 and 0.345 W for higher and lower voltage, respectively. The two different XRF tube configurations provided the two XRF data scenarios evaluated in this study.

For both voltage conditions, the fluorescence emission was measured during 90 s at atmospheric pressure. No filter was used in order to enhance the signal of light elements. A cellulose pellet was used as a blank sample, being scanned at the beginning of the measurements, after 50 samples, and at the end, to ensure the contaminant-free operation of the equipment. The spectra of the blank samples are shown in Figure A1, in the Appendix A.

The spectra were acquired using the Bruker S1PXR[®] software (Bruker AXS, Madison, EUA). The Bayesian deconvolution process was applied using Artax[®] (Bruker AXS, Madison, EUA) to correct peaks overlaps (inter-elemental effects). The spectra were normalized by the detector live time; then, they were presented in counts of photons per second (cps). The means of the spectra acquired using both tube voltage conditions are shown in Figure 2.

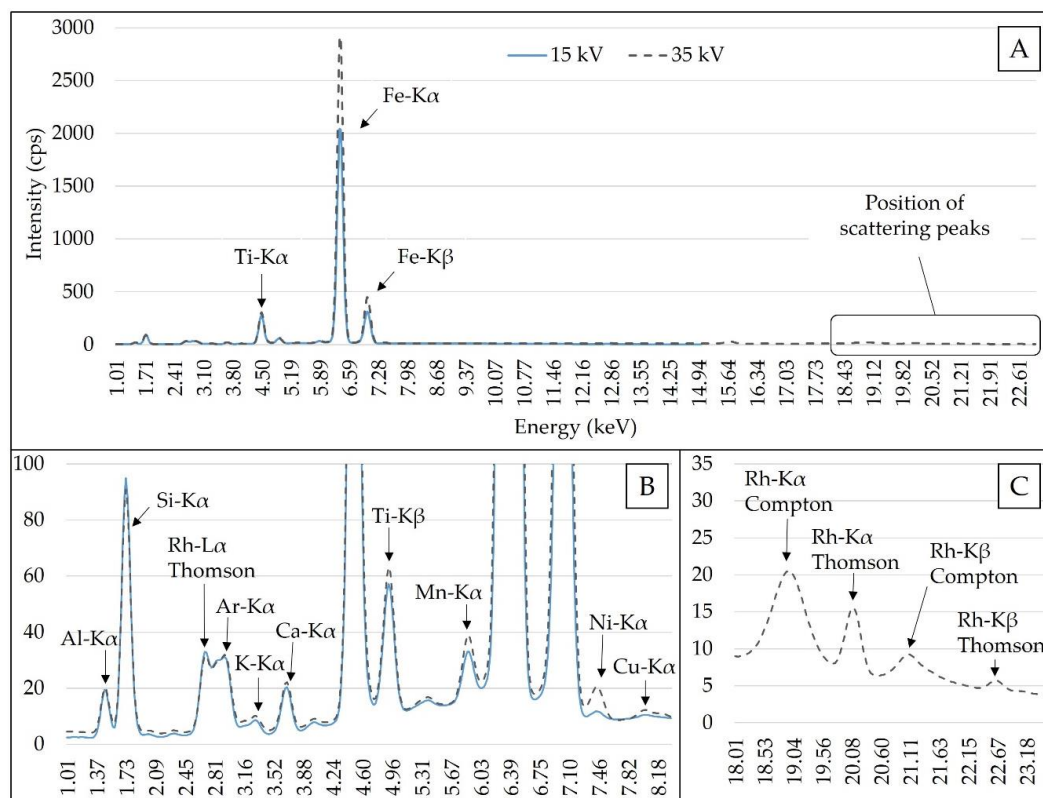


Figure 2. Mean of X-ray fluorescence (XRF) spectra obtained with an X-ray tube set at 15 and 35 kV (A). Snapshot of the emission lines from 1.01 to 8.34 keV, which presented lower fluorescence emission in relation to the K α emission lines of iron (Fe) and titanium (Ti) (B). Snapshot of scattering peaks (C). Counts of photons per second was abbreviated as cps.

The mean spectra were evaluated in order to select emission lines to be used as independent variables. This selection was based on the following criteria: (i) the element should be commonly found in agricultural soils; (ii) the signal-to-noise ratio (SNR) should be higher than 10 [37]; and (iii) for elements with K and L emission lines, just K-lines was chosen due to their greater fluorescence intensity. Following those criteria, nine fluorescence lines (K α emission lines of Al, Si, K, Ca, Ti, Mn, Fe, Ni, and Cu) and one scattering peak (Rh-L α Thomson) were selected in the 15 keV spectra (totalling 10 independent variables). For the 35 keV spectra, the same 10 lines were selected, including the two higher scattering peaks present in the region between 18 and 23 keV (totalling 12 independent

variables): Rh-K α Compton and Rh-K α Thomson. The 10 lines present in both spectra (Al-K α , Si-K α , K-K α , Ca-K α , Ti-K α , Mn-K α , Fe-K α , Ni-K α , Cu-K α , and Rh-L α) were compared through box-plot graphs.

Net intensities of the emission lines selected in the two different XRF data scenarios were used to build the predictive models. The XRF data scenarios using the 15 and 35 keV spectra were designated in this work as EL-15 and EL-35, respectively.

2.4. Modelling

Each one of the two XRF data scenarios (EL-15 and EL-35) was pulled in one matrix with the key fertility attributes (clay, OM, CEC, pH, V, re-P, ex-K, ex-Ca, and ex-Mg), measured via the above detailed commercial laboratory procedures. Calibration models were built using multiple linear regressions (MLR), as suggested by Weindorf and Chakraborty [12], using the Unscrambler[®] version 10.5.1 (Camo AS, Oslo, Norway). Calibration models were developed for each of the studied soil fertility attributes. The two-field dataset ($n = 102$) was divided into two subsets by means of the Kennard Stone algorithm [38], to 70% of data used for calibration and the remaining 30% used for validation. Descriptive statistical analyses were applied to characterize the variability of fertility attributes of both calibration and validation datasets. The methodology applied in this work was diagrammatically presented in Figure 3. The importance of XRF variables for the prediction of each fertility attribute was evaluated by the standardized regression coefficients of the regression analysis.

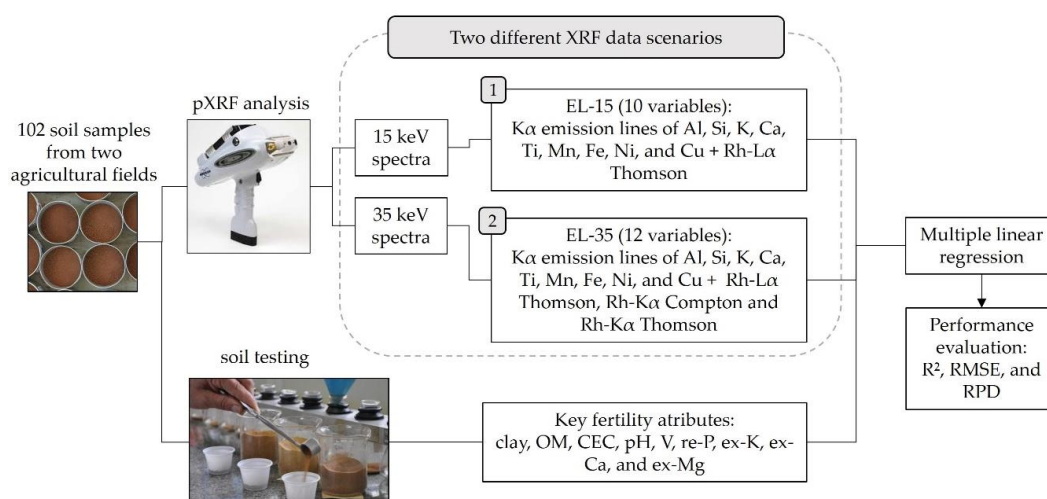


Figure 3. Framework of the methodology applied for the development of calibration models for clay, organic matter (OM), cation exchange capacity (CEC), pH, base saturation (V), resin-extracted (re-) P, and exchangeable (ex-) K, Ca, and Mg using an X-ray fluorescence (XRF) sensor configured with two different X-ray tube voltages (15 and 35 kV). For the X-ray tube set at 15 kV, 10 XRF lines were selected, comprising the K α emission line of aluminium (Al), silicon (Si), potassium (K), calcium (Ca), titanium (Ti), manganese (Mn), iron (Fe), nickel (Ni), copper (Cu), and the scattering peak Rh-L α Thomson; this XRF scenario was called EL-15. For the X-ray tube set at 35 kV, in addition to these 10 XRF lines, Rh-K α Compton and Thomson scattering peaks were included, this second scenario was called EL-35.

The quality of the developed calibration was assessed by means of the coefficient of determination (R^2), the residual prediction deviation (RPD), and the root-mean-square error (RMSE). Furthermore, we also used the normalized RMSE calculated by dividing the RMSE values by the range of each corresponding soil attribute. The RMSE was expressed in the units of the attribute of interest and in percentage, in the case on the normalized RMSE. The RPD was calculated as the ratio between the standard deviation of the laboratory measured soil property of interest and the RMSE in the prediction. The RMSE (%) and the RPD were used to compare the prediction performance of attributes that had

different scales and units of measurement. Four RPD classes adapted from Chang et al. [39] were used to evaluate the quality of the model prediction performance as poor models ($RPD < 1.40$), reasonable models ($1.40 \leq RPD < 2.00$), good models ($2.00 \leq RPD < 3.00$), and excellent models ($RPD \geq 3.00$).

3. Results

3.1. Laboratory Measured Soil Properties

The descriptive statistics of the fertility attributes for the calibration and validation datasets are shown in Table 1. The selection of the calibration and validation set should be wisely done to avoid the influence of different range or standard deviation (SD) of the two sets on the prediction accuracy and the introduction of greater prediction errors [40]. In this study, the range and SD for both calibration and validation datasets are comparable. This was only not the case for re-P, whose maximum value in the validation set (59.00 mg dm^{-3}) is explicitly lower than that in the calibration set ($104.00 \text{ mg dm}^{-3}$), with smaller SD (15.98 mg dm^{-3}) for the calibration set compared to that of the validation set (10.65 mg dm^{-3}).

The kurtosis and skewness values obtained for sample distribution analysis shown in Table 1 indicate that the samples of the dataset used were not normally distributed. In the proximal soil sensing context, data modeling using sets with uneven sample distribution is common [17,41]; however, this will introduce the Dunne effect with potential reduction in the prediction quality, as reported by Mouazen et al. [41].

Table 1. Descriptive statistics of fertility attributes for the calibration and validation dataset.

	Clay	OM ³	CEC ⁴	pH	V ⁵	re-P ⁶	ex-K ⁷	ex-Ca ⁷	ex-Mg ⁷
	— g dm ⁻³ —		mmol _c dm ⁻³		%	mg dm ⁻³	— mmol _c dm ⁻³ —		
Calibration set (n = 68)									
Min	175.00	14.00	37.50	4.60	19.00	4.00	0.90	8.00	3.00
1st Qu.	251.00	19.00	60.03	5.00	43.50	12.00	1.00	16.00	7.00
Mean	352.00	24.78	81.75	5.38	64.99	22.65	3.41	35.69	18.06
3rd Qu.	431.00	30.75	98.58	5.78	84.00	31.5	5.68	49.75	28.00
Max	511.00	37.00	148.90	6.30	92.00	104.00	10.30	78.00	54.00
SD ¹	95.21	6.13	25.86	0.47	21.96	15.98	2.48	19.08	12.58
CV ² (%)	27.05	24.72	31.63	8.67	33.80	70.55	72.73	53.44	69.65
Skewness	-0.22	0.14	0.46	0.50	-0.57	2.26	0.59	0.25	0.81
Kurtosis	-1.22	-1.10	-0.41	-1.02	-1.16	8.75	-0.79	-1.01	-0.14
Validation set (n = 34)									
Min	175.00	18.00	42.50	4.70	28.00	7.00	0.90	8.00	3.00
1st Qu.	226.00	22.00	53.08	4.90	39.00	12.00	1.18	13.00	5.00
Mean	332.12	26.62	76.50	5.21	64.15	19.09	3.36	33.32	17.50
3rd Qu.	406.25	32.00	98.90	5.50	86.25	21.00	5.50	51.25	30.00
Max	463.00	35.00	138.40	6.20	91.00	59.00	7.90	75.00	47.00
SD ¹	92.03	5.48	26.14	0.37	23.42	10.65	2.26	19.71	12.81
CV ² (%)	27.71	20.58	34.17	7.07	36.51	55.79	67.39	59.16	73.22
Skewness	-0.45	-0.11	0.53	0.83	-0.35	2.16	0.35	0.34	0.63
Kurtosis	-1.39	-1.45	-0.63	0.26	-1.62	5.78	-1.35	-1.11	-0.73

¹ Standard deviation, ² coefficient of variation, ³ organic matter, ⁴ cation exchange capacity, ⁵ base saturation, ⁶ resin-extracted P, and ⁷ exchangeable (ex-) nutrients (ex-K, ex-Ca, and ex-Mg).

In general, the soil samples were characterized by a high variability of all fertility attributes, with a coefficient of variation (CV) larger than 23%, with the only exception being for pH (CV < 8%). Despite the lower pH CV, a reasonable range of variation between very low and high [42] can be observed. Clay content varied from 175.00 to 511.00 g dm⁻³. According to the local fertility interpretation [42], the contents of re-P, ex-K, ex-Ca, and ex-Mg range from low to very high. We also noticed that by

joining data from both fields, the resulting dataset has a continuum range of values for all fertility attributes (Figure A2), which allows its modelling as a single dataset.

A significant correlation exists between the extractable and pseudo total contents of K, Ca, and Mg ($0.75 \leq r \leq 0.90$), whereas weak correlations were observed for P ($r = 0.11$). These significant correlations suggest that the exchangeable fractions of K, Ca and Mg can be assessed by XRF using the total content values, once their emission line is detected.

Interpreting the interrelationships between different fertility attributes (shown in Table 2) aid to understand why indirect (having no emission lines) predictions are still possible with XRF sensor data. Strong relationships exist between ex-Ca and ex-Mg ($r = 0.93$), as well as between each of them with V and CEC ($r \geq 0.84$). Positive correlations of CEC, V, ex-K, ex-Ca, and ex-Mg with clay range from 0.64 to 0.81. It should also be highlighted that re-P and pH showed weak to reasonable correlations with all the other attributes, with r ranging from -0.22 to 0.10 for re-P, and from -0.41 to 0.53 for pH. Finally, OM content has reasonable correlations with almost all attributes (except re-P and pH), with r ranging from -0.65 to 0.62 .

Table 2. Correlation matrix of the studied soil fertility attributes. Correlations between extractable and pseudo total content (ptc) for the different macronutrients are also shown.

	Clay	OM ¹	CEC ²	pH	V ³	re-P ⁴	ex-K ⁵	ex-Ca ⁵	ex-Mg ⁵
Clay	1.00	0.59 **	0.67 **	0.38 **	0.81 **	-0.06	0.73 **	0.78 **	0.64 **
OM		1.00	0.43 **	-0.01	0.62 **	0.07	0.48 **	0.55 **	0.44 **
CEC			1.00	0.42 **	0.76 **	0.02	0.64 **	0.93 **	0.93 **
pH				1.00	0.53 **	-0.22 *	0.40 **	0.46 **	0.44 **
V					1.00	-0.12	0.71 **	0.92 **	0.84 **
re-P						1.00	-0.1	0.01	-0.17
ex-K							1.00	0.68 **	0.58 **
ex-Ca								1.00	0.93 **
ex-Mg									1.00
Correlation with ptc						0.11	0.90 **	0.75 **	0.83 **

¹ Organic matter, ² cation exchange capacity, ³ base saturation, ⁴ resin-extracted P, and ⁵ exchangeable (ex-) nutrients (ex-K, ex-Ca, and ex-Mg). * Significant correlation at the probability level of 0.05; ** Significant correlation at the probability level of 0.01; the correlations were presented on grayscale highlighting the highest values, which were evaluated ignoring the sign (module).

3.2. Effect of X-ray Tube Configuration on XRF Emission Lines

The intensity of the emission lines present in both EL-15 and EL-35 scenarios [namely, Al-K α , Si-K α , Rh-L α (Thomson), K-K α , Ca-K α , Ti-K α , Mn-K α , Fe-K α , Ni-K α , and Cu-K α] are plotted in box-plot graphs (Figure 4), allowing comparison between them, as a function of the X-ray tube configuration. All the emission lines presented a high correlation coefficient ($r > 0.90$) between EL-15 and EL-35. The largest deviation was observed for Ni-K α , with $r = 0.73$. This lower correlation was influenced by the low dispersion and intensity of the Ni-K α XRF emission in EL-15.

The X-ray tube configuration affected the intensity of the emission lines of the different elements detected in both XRF scenarios. The K α emission lines of the light elements Si and Al, with atomic number (Z) of 13 and 14, respectively, presented higher intensity when using the tube configured at 15 kV (EL-15) than using that configured at 35 kV (EL-35) (Figure 4a,b, respectively). The emission lines of K and Ca (with atomic numbers of 19 and 20, respectively) showed, in both scenarios (EL-15 and EL-35), a very similar intensity and dispersion of XRF emission (Figure 4d,e, respectively). However, Ti, Mn, Fe, Ni, and Cu (with atomic numbers 22, 25, 26, 28, and 29, respectively) showed higher XRF emission in the EL-35 scenario than that of the EL-15 (Figure 4f-j, respectively).

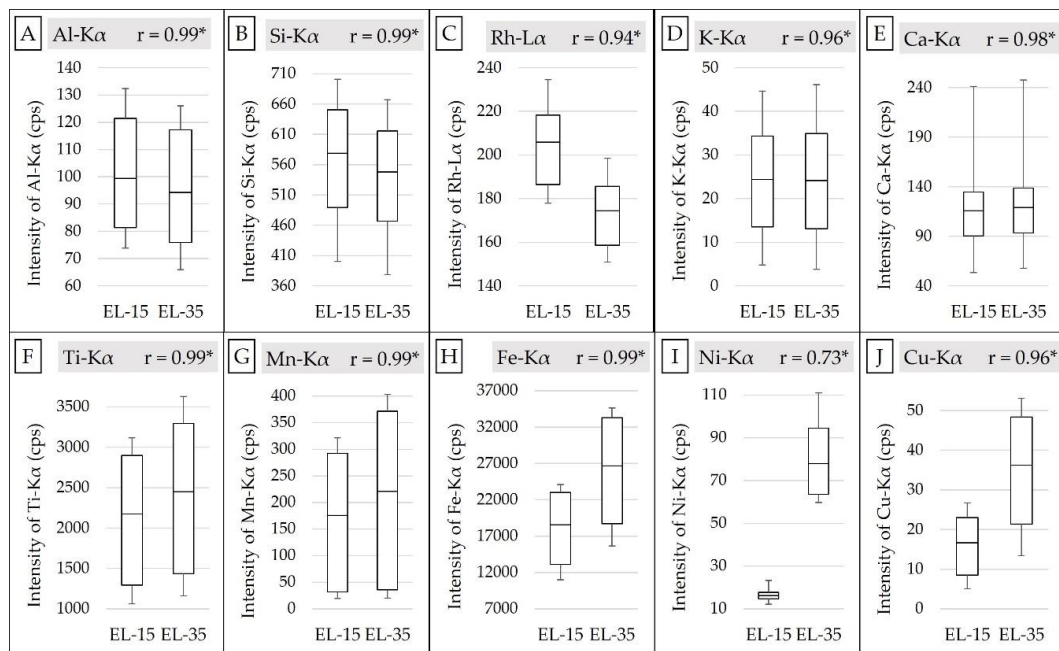


Figure 4. Box plot of the intensity of the lines Al-K α , Si-K α , Rh-L α , K-K α , Ca-K α , Ti-K α , Mn-K α , Fe-K α , Ni-K α , and Cu-K α ((A–J), respectively) obtained using a portable X-ray fluorescence (XRF) sensor configured with two different X-ray tube voltages (15 and 35 kV). The XRF scenario using the X-ray tube set at 15 kV is named EL-15 and the XRF scenario using the X-ray tube set at 35 kV is named EL-35. The Pearson correlation between the EL-15 and EL-35 is also presented (correlations followed by * were significant at the probability level of 0.01).

3.3. Effect of X-ray Tube Configuration on pXRF Performance

The MLR prediction accuracy for the studied fertility attributes is similar between the EL-15 and EL-35 models (Table 3). The biggest differences were obtained for OM and pH, with R^2 values of 0.61 and 0.72, and 0.27 and 0.38, for EL-15 and EL-35, respectively. The prediction results for the remaining attributes are comparable with differences in R^2 values less than 0.06 between EL-15 and EL-35.

Table 3. Prediction results of the validation set ($n = 34$) obtained from multiple linear regressions (MLR) models calibrated using a portable X-ray fluorescence (XRF) sensor configured with two different X-ray tube voltages of 15 and 35 kV, designated as EL-15 and EL-35, respectively.

	Clay	OM ¹	CEC ²	pH	V ³	re-P ⁴	ex-K ⁵	ex-Ca ⁵	ex-Mg ⁵
R^2									
EL-15	0.88	0.61	0.80	0.27	0.95	0.00	0.90	0.91	0.85
EL-35	0.91	0.72	0.75	0.38	0.96	0.03	0.90	0.91	0.83
RMSE									
EL-15	34.7	3.55	10.42	0.36	4.83	13.86	0.71	5.74	4.88
EL-35	31.72	2.87	11.08	0.32	4.82	13.41	0.65	5.63	4.97
RMSE (%)									
EL-15	12.05	20.87	10.86	24.15	7.66	26.65	10.16	8.56	11.09
EL-35	11.01	16.87	11.55	21.17	7.65	25.79	9.31	8.40	11.29
RPD									
EL-15	2.65	1.54	2.51	1.02	4.85	0.77	3.18	3.44	2.63
EL-35	2.90	1.91	2.36	1.16	4.86	0.79	3.47	3.50	2.58

¹ Organic matter; ² cation exchange capacity; ³ base saturation; ⁴ resin-extracted P; ⁵ exchangeable (ex-) nutrients (ex-K, ex-Ca, and ex-Mg). The coefficient of determination (R^2) and residual prediction deviation (RPD) values are presented on grayscale, highlighting the highest values. The root-mean-square error (RMSE) was given in g dm^{-3} for clay and OM; in mmolc dm^{-3} for CEC, ex-K, ex-Ca, and ex-Mg; in % for V; and, for re-P, the RMSE was given in mg dm^{-3} . The scatter plots of measured versus predicted fertility attributes are included as an annex (Figure A2).

The similarity between both XRF tube voltage data scenarios is also noted when analyzing the importance of the independent variables (X-variables) in both XRF scenarios, since the most important variables were always coincident in the prediction models calibrated with EL-15 and EL-35 (Table 4). More specifically, in both scenarios, Fe-K α was the main variable for clay prediction, Mn-K α for OM, K-K α for ex-K, and Ca-K α for CEC, V, ex-Ca, and ex-Mg. It is also observed that neither the Rh-K α Compton and Thomson scattering peaks—present only in EL-35—nor the Ni-K α were the main X-variable in any of the calibrated models (Table 4), which also contribute to the similarity between the predictive models calibrated with both X-ray tube configurations.

Table 4. Importance of X-ray fluorescence (XRF) variables for the prediction of studied soil fertility attributes, using the two XRF tube voltage data scenarios of EL-15 and EL-35, designated as EL-15 and EL-35, respectively. The values presented correspond to the t-value for each standardized coefficient obtained in the regressions calibration.

	Clay	OM ¹	CEC ²	pH	V ³	re-P ⁴	ex-K ⁵	ex-Ca ⁵	ex-Mg ⁵
EL-15									
Al-K α	-1.35	1.48	0.11	-1.48	-0.21	-1.73	-2.83	0.21	1.29
Si-K α	-2.07	-0.71	-0.37	-0.83	2.04	-0.94	-2.40	2.26	2.07
K-K α	-1.13	-1.36	1.50	2.20	-0.25	0.07	14.75	0.86	0.27
Ca-K α	-0.20	1.24	5.03	2.90	7.49	1.23	-5.95	9.35	7.10
Ti-K α	-2.31	-2.54	3.58	2.05	-0.46	-2.55	0.01	1.55	5.41
Mn-K α	-0.71	3.54	-1.79	-0.73	0.34	0.49	-0.83	-2.16	-2.48
Fe-K α	9.22	-0.63	-0.57	-0.20	2.49	-0.40	1.98	2.60	-1.12
Ni-K α	-0.09	-0.26	-0.05	0.03	0.59	2.81	0.37	0.41	-0.80
Cu-K α	-1.77	0.44	0.26	-1.51	-1.84	3.32	-1.53	-0.09	-1.16
Rh-L α Thomson	0.52	1.97	0.23	-3.22	1.97	0.20	-4.06	2.28	1.73
EL-35									
Al-K α	-1.14	0.93	-0.48	-0.24	-0.90	-0.55	-1.01	-1.11	-0.91
Si-K α	-2.08	0.53	-0.73	-1.17	0.23	0.29	-0.81	0.52	-0.17
K-K α	-1.20	-0.43	1.46	2.04	0.22	-0.65	18.89	0.92	0.41
Ca-K α	-0.27	1.11	4.45	3.33	7.89	1.09	-5.68	9.08	5.78
Ti-K α	-2.99	-1.91	2.73	1.30	-1.61	-1.61	-0.93	0.09	3.54
Mn-K α	-0.40	2.59	-1.77	-0.14	0.74	0.64	-1.97	-1.92	-1.96
Fe-K α	5.09	0.50	-0.27	-1.55	0.19	0.38	-1.42	0.64	-0.34
Ni-K α	-1.12	-0.73	1.26	-0.07	0.09	1.44	-0.49	1.13	0.75
Cu-K α	-1.30	0.42	0.90	-2.00	-1.85	3.54	-0.64	0.65	-0.94
Rh-L α Thomson	-1.07	2.32	-0.88	-2.40	1.02	0.27	-4.27	0.65	-0.50
Rh-K α Thomson	0.38	0.23	-0.25	0.90	1.78	-1.02	-1.02	1.27	0.22
Rh-K α Compton	-0.61	1.07	-0.43	-1.83	-1.79	1.13	-2.38	-1.46	-0.63

¹ Organic matter; ² cation exchange capacity; ³ base saturation; ⁴ resin-extracted P; ⁵ exchangeable (ex-) nutrients (ex-K, ex-Ca, and ex-Mg). The emboldened values indicate a significant correlation at the probability level of 0.05; significant values were presented on grayscale, with the most important variables having the darkest colour and vice versa.

3.4. pXRF for Key Fertility Attributes Prediction

In general, satisfactory predictions (RPD > 1.40 and R² ranging from 0.61 to 0.96) were observed in the following order: V > ex-Ca \geq ex-K > clay > ex-Mg > CEC > OM. However, predictions of pH and re-P were rather poor (RPD < 1.4 and R² \leq 0.38).

For clay predictions, the RPD ranges of 2.65–2.90 and the independent variables Fe-K α , Si-K α , and Ti-K α contributed significantly to both XRF scenarios (Table 4), with the Fe-K α being the most important one, presenting the highest standardized coefficient. Models for OM showed reasonable prediction performances, with RPD values of 1.54 and 1.91 for EL-15 and EL-35, respectively. The most important independent variables in OM models were Mn-K α and Ti-K α , for EL-15, and Mn-K α and Rh-K α Thomson, for EL-35 (Table 4), with the Mn-K α emission line being the most significant standardized coefficient in both scenarios.

Models for ex-K and ex-Ca were excellent, with RPD higher than 3.00 in both scenarios. The $K\alpha$ emission line of K and Ca were the main independent variables (with the greatest standardized coefficient) (Table 4). Therefore, the excellent predictive models for ex-K and ex-Ca is justified by the significant correlation between the extractable and pseudo total content of K ($r = 0.67$) and Ca ($r = 0.83$) present in this dataset (Table 1).

Models for CEC, V, and ex-Mg achieved good and excellent prediction performances, with RPD ranging from 2.36 to 2.63, for CEC and ex-Mg, and from 4.85 and 4.86 for V. For both XRF scenarios, the main X-variable contributing to all these properties (including pH) was the Ca- $K\alpha$. It is interesting to note that the prediction performance of pH, CEC, V, and ex-Mg was related to the correlation of these variables with the ex-Ca content (Figure 5). One can observe that CEC, V, and ex-Mg properties, having satisfactory prediction performance ($R^2 \geq 0.75$), are high correlated with ex-Ca ($r > 0.90$). The lower correlation between pH and ex-Ca ($r = 0.46$), however, explains the poor prediction performance ($R^2 < 0.40$) for pH.

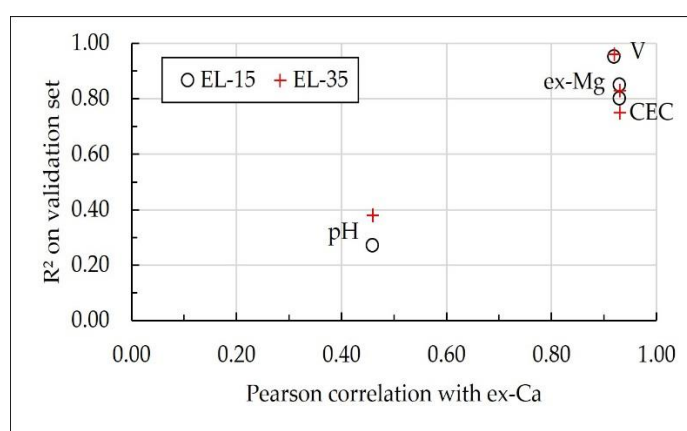


Figure 5. Scatter plot of the determination coefficient (R^2) obtained on the validation set of models calibrated for cation exchange capacity (CEC), pH, base saturation (V), and exchangeable (ex-) Mg versus the correlation coefficient (r) of each mentioned attribute with the ex-Ca content. The relationships for the XRF data scenarios EL-15 and EL-35 are represented by circles and crosses, respectively.

4. Discussion

4.1. Performance Regarding the X-ray Tube Configuration

The X-ray tube anode emits a continuous spectrum when it is struck by accelerated electrons [43]. Essentially, when the voltage of the tube is increased, it also increases: (i) the energy range of the continuous spectrum; (ii) the overall emission intensity of the continuous spectrum; and (iii) the energy at maximum intensity in the continuous spectrum [29]. In parallel, when increasing the current applied to the X-ray tube, increments only in the intensity of the continuous spectrum are observed, since the photon flow is increased [30]. A schematic figure illustrating the behavior of the continuous spectrum emitted by the X-ray tube when modifying its voltage and current is presented in the Appendix A (Figure A3).

Different configurations of X-ray tube—with different combinations of voltage and current—change the continuous spectrum emitted by the X-ray tube and, therefore, the fluorescence behavior emitted by the elements present in the sample [29]. The results of this research show that the intensity of XRF emission of the different elements was indeed influenced by the configuration of the X-ray tube (Figure 4). Nevertheless, the emission lines detected in both the EL-15 and EL-35 scenarios [namely, Al- $K\alpha$, Si- $K\alpha$, Rh- $L\alpha$ (Thomson), K- $K\alpha$, Ca- $K\alpha$, Ti- $K\alpha$, Mn- $K\alpha$, Fe- $K\alpha$, Ni- $K\alpha$, and Cu- $K\alpha$] showed significant correlation with each other (Figure 4), while Ni- $K\alpha$ showed the smallest correlations between the EL-15 and EL-35 scenarios (Figure 4I). The reduced intensity and dispersion of Ni XRF emission in

EL-15 (Figure 4I) can be explained by the short energy range that is able to excite Ni ($K_{\text{edge}} = 8.33 \text{ keV}$) when the tube was set at 15 kV. In turn, for the EL-35, the Ni XRF emission was favored, similar to that observed for elements with an absorption edge close to Ni (e.g., Fe and Cu). In addition to that, it is important to highlight that part of the Ni signal is coming from the equipment itself (as can be seen in Figure A1); hence, it is also highly affected by the tube configuration.

X-ray tube configurations that produce continuous radiation with peak intensity closer to the absorption edge of light elements (e.g., 1.30, 1.56, 1.84, and 2.15 keV, representing the K edge of Mg, Al, Si, and P, respectively) benefit the XRF emission of these elements [31,43]. Therefore, it is expected that the EL-15 configuration would promote better predictions of light elements, such as ex-K and ex-Ca. However, the results obtained in this study do not support this assumption. The performance of the two X-ray tube configurations was very similar, even for the prediction of ex-K and ex-Ca, whose prediction models had a great weight of the emission lines of light elements (K- $K\alpha$ and Ca- $K\alpha$, respectively). Working on tropical soils, Silva et al. [24] compared different operational modes (Trace Mode and General Mode) of a pXRF sensor (using a Bruker, S1 Titan LE, Bruker, Madison, USA) for the prediction of ex-Ca, observing slight variations in performance ($0.77 \leq R^2 \leq 0.85$) for ex-Ca prediction when comparing both operational modes. Although the details of the X-ray tube configuration of the operational modes evaluated are not disclosed, it is common that the instrumental conditions for “trace” analysis use low voltage and high current, similar to the EL-15 scenario applied in this work. Thus, this subtle oscillation of prediction performance due to changing the XRF operational mode observed by Silva et al. [25] can be compared to the results shown in the present study.

The minimal effect of both X-ray tube configurations on the prediction of fertility attributes may well be explained by the low importance of the X-variables Rh- $K\alpha$ Compton, Rh- $K\alpha$ Thomson (scattering peaks present in the region between 18 and 23 keV), and the Ni- $K\alpha$. If these variables had a higher weight on the regression of some attribute, more relevant differences might be possible. The scattering peaks can be useful independent variables for OM prediction, as observed by Morona et al. [19], and after normalization of XRF emission lines to attenuate the matrix effect [44].

The spectra observed in this research did not present emission lines for Mg and P due to their low XRF intrinsic sensitivity (e.g., lower fluorescence yield) and low Si-detector efficiency at this photon energy range, which is translated in high limits of detection. In this work, the greatest ptc of Mg and P were, respectively, 789.65 and 669.18 mg kg^{-1} , corresponding to an extractable content of 54 $\text{mmol}_c \text{ dm}^{-3}$ and 104 mg dm^{-3} for ex-Mg and re-P, respectively. X-ray tube configurations with energy levels below 15 kV should be further investigated for the detection of Mg and P, as they can promote more efficient excitation of these elements in soil samples [31]. By further reducing the X-ray tube voltage setting, the intensity of the continuous spectrum in low energies is increased, as well as the limit of detection of low Z elements being reduced. Potts et al. [31], working with an ED-XRF in rock powder samples, observed that Mg, Si, and Ca are most efficiently excited when using the X-ray tube configured at low energies (e.g., 6–8 kV).

In view of our results, both scenarios of X-ray tube configuration (EL-15 and EL-35) can be used for predicting the studied fertility attributes, since their prediction results were comparable. Nevertheless, it is important to point out that some studies suggested that the information at the scattering region between 18 and 23 keV that is present only in spectra obtained with the Rh-tube configured at voltages above 23 kV may be promising for the prediction of organic attributes (Morona et al. [19]) and for the matrix effect attenuation using the Compton normalization [29].

4.2. pXRF Models Performance for the Prediction of Key Fertility Attributes

Simple linear regressions and MLR are approaches traditionally used to model XRF data for predicting soil physicochemical attributes [12]. In this work, the net intensities of XRF emission lines, which were previously selected (as mentioned in the Section 2.3.), were used to build the predictive models by means of MLR. The main difference between the method used in this study and those in the most of the studies that used XRF sensors to predict soil fertility attributes [13–15,20–22,25–27] is

that it does not use pre-programmed measurement packages for spectra acquisition and processing. These packages allow quantifying the total contents of different elements present in the samples, in the form of oxides (e.g., MgO, CaO, SiO₂, K₂O, Al₂O₃, among others), which are then subjected to calibration models for the fertility attributes prediction. As an alternative, we propose a simple and transparent methodology for XRF data acquisition and processing, which proved in this work to provide satisfactory prediction results ($0.61 \leq R^2 \leq 0.96$) for clay, OM, CEC, V, ex-K, ex-Ca, and ex-Mg (Table 3), with the exception being for pH and re-P, which gave poor results ($R^2 \leq 0.38$). In addition, we confirm that the results obtained in this work are comparable to those obtained by other researchers using pre-programmed measurement packages, which are discussed below for each fertility attribute.

Predictions of clay demonstrated good performance ($0.88 \leq R^2 \leq 0.91$ and $2.65 \leq RPD \leq 2.90$). Some studies have already reported satisfactory predictions of texture attributes via XRF sensor [13,24,45]. In Brazilian tropical soils, Lima et al. [45] and Silva et al. [24] observed satisfactory prediction performance for clay, with R^2 ranging from 0.71 to 0.85. The successful prediction of clay content in tropical soils is explained by its relationship with the total content of Al, Fe, and Si, which are constituents of clay minerals, e.g., kaolinite [Al₂Si₂O₅(OH)₄], gibbsite [Al(OH)₃], hematite (α -Fe₂O₃) and goethite (FeOOH) [45,46]. Eventually, other cations, like microelements (Ni, Cr, Co, Cu, Zn, Ti, etc), can also be present in the iron oxides structure as isomorphous substitutes for Fe [47]. In this work, the main contributing X-variable for predicting the clay content was the Fe-K α , with the K α -lines of Ti and Si (Table 4) being secondary contributing variables.

The reasonable prediction results for OM ($0.61 \leq R^2 \leq 0.72$ and $1.54 \leq RPD \leq 1.91$) can be attributed to OM's significant correlation with clay, ex-Ca, and ex-K (Table 1), all predicted with good accuracy with XRF. In tropical soils, different researchers have reported satisfactory predictions for OM, with R^2 ranging from 0.48 to 0.98 [20,21,45]. Morona et al. [21] suggested using the energy range of 18–30 keV to establish calibration models for OM. This is because the organic compounds of soil are essentially light elements (H, C, N and O), having no emission lines to be detected by ED-XRF technique, and the scattering peaks carry information of these elements [21]. It is well-known that the intensity of the XRF scattering energy is inversely related to the average atomic number of the sample [44]. Thus, increasing OM will decrease the average atomic number of the sample and will trend increase the ratio between Rh-K α Compton and Rh-K α Thomson. Despite the significant relationships between OM and scattering peaks, observed by Morona et al. [19], the results of this study do not show the same. In the current study, the important variables for OM predictions were Mn-K α and Ti-K α , for EL-15, and, Mn-K α and Rh-K α Thomson, for EL-35 (Table 4). Other research suggested that satisfactory predictive models can be obtained for OM if it is correlated with texture attributes [45], which is a common correlation found for tropical soils [42].

Excellent prediction results for ex-Ca and ex-K were observed, with R^2 ranging from 0.90 to 0.91, and $RPD > 3.00$. The total content of Ca and K were the main X-variables for the prediction of their exchangeable contents (Table 4). Andrade et al. [21] observed similar behaviour in tropical soils. The correlation between extractable and total contents is the main reason to justify the use of an XRF emission line of a given nutrient for the prediction of its respective extractable contents [48]. The sample set used in this work presented a significant correlation ($r \geq 0.75$) between the pseudo total and the exchangeable contents of Ca and K (Table 1). Satisfactory prediction results ($R^2 = 0.71 - 0.89$) of ex-Ca in tropical soils via XRF were observed by different authors [20–22,25]. Models of ex-K in Brazilian tropical soils have been reported less frequently in the literature. Studies conducted by Silva et al. [20] and Andrade et al. [21] showed satisfactory prediction performance for different soil types, with R^2 of 0.81 and 0.67, respectively. In contrast, Teixeira et al. [22] reported poor predictive models of ex-K ($0.04 \leq R^2 \leq 0.12$) using tropical soil samples acquired from areas with different land uses. This different quality of model prediction performance between ex-K and ex-Ca can be attributed to the different degrees of correlation between the total and extractable fractions.

Due to the weathered nature of tropical soils, their composition often shows an irrelevant presence of primary minerals (natural source of nutrients) [49]. Consequently, the relationships between the total and extractable contents of some nutrients (e.g., ex-Ca, ex-K, and ex-Mg) are mainly influenced by soil agricultural management rather than natural processes [21,45]. This characteristic of tropical soils is attractive to encourage using XRF sensors for the prediction of extractable nutrients. On the other hand, in soils with the presence of phyllosilicates integrated with other soil minerals—such as mica (natural source of K) or calcite (natural source of Ca)—the relationship between the total and extractable content is more unlikely to occur; hence, models involving XRF spectra may not show positive results. The soil chemistry in tropical soils regarding P is complex and characterized by high levels of P associated with strong bonds to Fe oxides (hematite and goethite) and Al (gibbsite). This complexity unbalances the relationship between its total content present in the soil and the amount of P accessible to plants [46,50]. The data of the present research showed a weak correlation ($r = 0.11$) between the re-P and its pseudo total content (Table 1). The prediction for re-P in this study was poor ($R^2 \leq 0.03$ and $RPD \leq 0.79$); however, it could perform better if this attribute had good correlations with other fertility attributes (e.g., textural attributes, ex-K, or ex-Ca), predicted successfully by XRF. In Brazilian tropical soils, studies conducted by Andrade et al. [21] and Lima et al. [45] showed poor performance ($R^2 < 0.25$) for extractable P predictions. Teixeira et al. [22], evaluating soils from agricultural and native areas, reported variable prediction results of extractable P, with R^2 ranging from 0.03 to 0.90. The best models obtained by Teixeira et al. [22] were built using soil samples collected from different agricultural fields.

Good prediction results were observed for CEC and ex-Mg ($0.75 \leq R^2 \leq 0.85$ and $2.36 \leq RPD \leq 2.63$) and excellent predictions for V ($0.95 \leq R^2 \leq 0.96$ and $4.85 \leq RPD \leq 4.86$). The Ca-K α emission line was found as the main variable for the prediction of CEC, ex-Mg, and V (Table 4). Satisfactory prediction performance of ex-Mg in tropical soils was also reported by Silva et al. [20] and Andrade et al. [21], with R^2 of 0.85 and 0.60, respectively; both studies reported that Ca was the most important variable. Teixeira et al. [22] reported R^2 ranging from 0.08 to 0.89 for V models in tropical soils, observing that Ca (CaO in that work) was the main prediction variable. Silva et al. [20] obtained good results for V and CEC, with R^2 ranging from 0.81 to 0.89, and from 0.86 to 0.87, respectively, indicating that CaO information was the main variable for CEC prediction.

It is observed that models calibrated for CEC, pH, V, and ex-Mg (all having Ca-K α as their main X-variable) were influenced by the degree of the correlation with ex-Ca content (Figure 5). Therefore, the relationship between ex-Ca on one hand, and ex-Mg, CEC, pH, and V attributes on the other, can be explained by the lime application, a common practice in Brazilian agriculture. The lime application promotes the neutralization of part of the soil acidity (related to H^+ e Al^{3+}) that releases negative charges on the soil exchange complex, and then these charges are occupied by nutrients, such as Ca^{2+} , Mg^{2+} and K^+ [51,52]. This soil management can increase the levels and concentration of pH, CEC, V, ex-Ca, and ex-Mg [53], hence increasing the probability of correlations between them. Both fields in this study received lime, explaining the strong correlations among them. However, the relationships between CEC, V, and ex-Mg are unlikely to be temporally stable, since they are altered depending on the soil management applied and other agronomical factors (e.g., weather conditions, crop development, etc.). Thus, the quality of XRF prediction performance of these attributes can also oscillate between different cropping seasons, which requires future investigations to understand the temporal stability of the XRF models.

The results presented in this work confirmed the potential of XRF to predict key fertility attributes in tropical soils. However, comparing results reported by different research, it becomes evident that the performance will vary according to the characteristics presented by the sample set (e.g., mineralogy and the interrelations between fertility attributes). Although the results of this work show satisfactory prediction performance by combining samples from two fields with contrasting texture characteristics, it is expected that different areas will not always have compatible sample sets (e.g., similar mineralogy). In order to better understand and control the local and temporal variability in the sample set, affecting the XRF performance to predict fertility attributes, future research is suggested to (i) evaluate the

stability of models over time (e.g., in different cropping seasons), and (ii) develop a methodology to determine fields (e.g., sample set) to be used for the best XRF prediction performance.

Recent studies have proposed the use of more sophisticated methods for modelling XRF data (e.g., partial least squares regression (PLSR), machine learning and computational models) to deal with the matrix effect, as well as to account for and extract hidden spectral information [32,54]. These modelling approaches can be promising for optimizing XRF data processing, especially for modelling datasets with a large number of soil samples. Hence, we also encourage future research that aim to optimize the XRF data modelling, using the mentioned approaches combined with transparent data acquisition routines for predicting fertility attributes.

4.3. Perspectives for Using XRF Sensors as a PSS Tool

Pre-programmed measurement packages are practical tools for XRF data acquisition and processing [28]; besides that, their application is associated with a pre-established scanning time (generally between 60 to 90 s [12]). This analysis time is quite contrasting when compared to the analysis time of other PSS techniques. For example, apparent electrical conductivity (ECa) and visNIRS techniques both allow a data acquisition frequency of 1Hz; hence, they are used for on-the-go applications. Another example is the ion-selective electrodes (ISE) sensor, using ISE systems adapted to on-the-go readings, which can operate at a data acquisition frequency of one datum every 15 s, which is limited by its stabilization time (about 10 s) [1].

The analysis time is decisive for the application of the XRF technique in on-site operations and in hybrid laboratories [1], it being interesting that it does not exceed 15s (the time generally used by on-the-go ISE systems). Reducing the analysis time of XRF sensors implies reducing the accuracy of the spectrum, due to noise increase [12]. However, fast analyses are already applied using the μ -XRF technique, which is a variant of the XRF technique, allowing for scanning the elements over the sample surface by employing a micrometric X-ray beam, which acquires spectra in high spatial density (e.g., about 350 spectra per mm^2) [11,55]. To make this assessment within an acceptable time, each X-ray spectrum is scanned for a very short period (e.g., 1 to 3 s per spectrum). The XRF data acquisition applied in this research used a scanning time of 90s for both X-ray tube conditions. However, the implementation of this methodology is independent of the scanning time, allowing its application under different dwell times (e.g., from 5 to 120s), which can be done only by changing the sensor configuration. Furthermore, using this data acquisition associated with the modelling procedure applied (MLR with selected emission lines) enables the optimization of the XRF scanning time, which should encourage future studies to evaluate the trade-off between the dwell time and the analytical performance for the prediction of fertility attributes.

Briefly, this research has shown that it is possible to predict soil fertility attributes using an Rh-anode X-ray tube configured at both 15 and 35 kV, since the observed performances of both XRF data scenarios were comparable to those presented by other studies that used pre-programmed measurement packages [20–22,25]. Nevertheless, it is also important to mention that only tubes configured at 35 kV have the Rh-scattering region between 18 and 23 keV, demonstrating promising relationships with fertility attributes in some cases (e.g., for OM, as reported by Morona et al. [19]). In addition, the procedure of data acquisition and modelling applied in this research is a simple and transparent methodology that enables further research that seeks to optimize the XRF scanning time in soil sample analyses. Such knowledge is important to develop new XRF sensor applications in the context of PSS (e.g., embedding XRF sensors in mobile platforms).

5. Conclusions

The X-ray tube configuration of an X-ray fluorescence (XRF) spectrometer affected the intensity of the emission lines of the different elements detected. By reducing the Rh-anode X-ray tube voltage from 35 to 15 kV and incrementing the tube current from 7 to 23 μ A (designated as EL-35 and EL-15 scenarios, respectively), increases in X-ray fluorescence emission intensity were observed for the Si and Al elements. The behavior of the $K\alpha$ emission lines of K and Ca elements showed no differences in both X-ray tube configurations tested. All other emission lines detected (namely, Ti- $K\alpha$, Mn- $K\alpha$, Fe- $K\alpha$, Ni- $K\alpha$, and Cu- $K\alpha$) were higher at 35 kV. Emission lines of P and Mg were not detected using any of the tested configurations.

Both XRF sensor configurations performed satisfactorily ($0.61 \leq R^2 \leq 0.96$) to predict clay, OM, CEC, V, and exchangeable K, Ca, and Mg, whereas the prediction results for pH and extractable P were unsatisfactory ($R^2 \leq 0.38$). The different XRF tube configurations (EL-15 and EL-35), applied in a Rh-anode X-ray tube, provided similar performances to predict all key fertility attributes evaluated. Therefore, data from this work support that both X-ray tube configurations can be used for predicting fertility attributes. However, it is important to note that only tubes configured at 35 kV have the Rh-scattering region between 18 and 23 keV, which may bring useful information in some datasets.

The methodology proposed in this work based on the multiple linear regression (MLR) modelling approach showed a comparable prediction performance to other published studies that relied on pre-programmed measurement packages for the XRF data acquisition and processing, a procedure that is associated with long scanning time (generally between 60 and 90 s) and is not compatible with proximal soil sensing (PSS) applications. It is suggested to use transparent and practical data acquisition methodologies such as reducing the XRF scanning time in order to speed up the XRF analysis in soil samples. This will be beneficial for research communities and commercial application in precision agriculture, soil science, and soil management, among others.

Author Contributions: Conceptualization, T.R.T., L.C.N., and J.P.M.; methodology, T.R.T., L.C.N., E.E.N.A., A.M.M., and F.L.M.; validation, L.C.N., E.E.N.A., and J.P.M.; formal analysis, T.R.T., L.C.N., E.E.N.A., A.M.M., and F.L.M.; investigation, T.R.T.; resources, T.R.T.; data curation, T.R.T.; writing—original draft preparation, T.R.T., and A.M.M.; writing—review and editing, E.E.N.A., F.L.M., H.W.P.d.C., A.M.M., and J.P.M.; visualization, T.R.T.; supervision, H.W.P.d.C., A.M.M., and J.P.M.; project administration, T.R.T., and J.P.M.; funding acquisition, T.R.T., J.P.M., and H.W.P.d.C. All authors have read and agreed to the published version of the manuscript.

Funding: The T.R.T. and E.E.N.A. were funded by São Paulo Research Foundation (FAPESP), grant number 2017/21969-0 and 2018/08877-2, respectively; and also partial funded by the Brazilian Federal Agencies: Coordination for the Improvement of Higher Education Personnel (CAPES)—Finance Code 001, and the National Council for Scientific and Technological Development. (CNPq). XRF facilities were funded by FAPESP, grant 2015-19121-8, and “Financiadora de Estudos e Projetos” (FINEP) project “Core Facility de suportes às pesquisas em Nutrologia e Segurança Alimentar na USP”, grant 01.12.0535.0. Authors also acknowledge the financial support received from the Research Foundation-Flanders (FWO) for Odysseus I SiTeMan Project (Nr. G0F9216N).

Acknowledgments: We would like to thank the technicians Fátima Patreze and Liz Mary Bueno de Moraes, from Analytical Chemistry Laboratory, for the support with the sample preparation; the technician Eduardo de Almeida, from Laboratory of Nuclear Instrumentation, for the support with X-ray fluorescence equipment; the Ph.D. fellow Felipe dos Santos Rodrigues, from the Laboratory of Applied Nuclear Physics (UEL), for the support in some data analysis; and, also the technician Marina Colzato, from the Laboratory of Environmental Analysis, for the support with soil analysis.

Conflicts of Interest: The authors declare no conflict of interest. The funders had no role in the design of the study; in the collection, analyses, or interpretation of data; in the writing of the manuscript, or in the decision to publish the results.

Appendix A

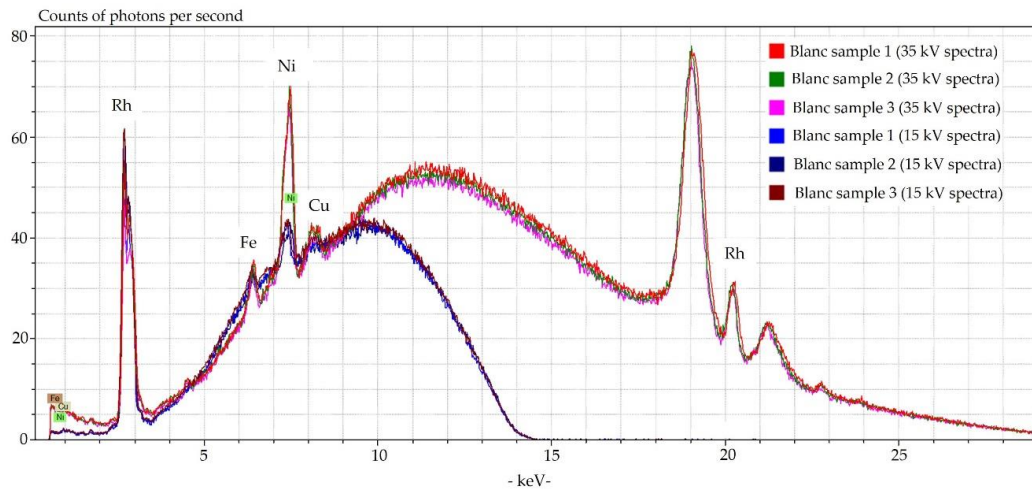


Figure A1. Spectra of the blank sample obtained during the XRF data acquisition using the X-ray tube configured at 15 and 35 kV. The spectra acquired at the beginning, after 50 samples, and at the end of the measurements are designated in the legend as Blanc sample 1, 2, and 3, respectively.

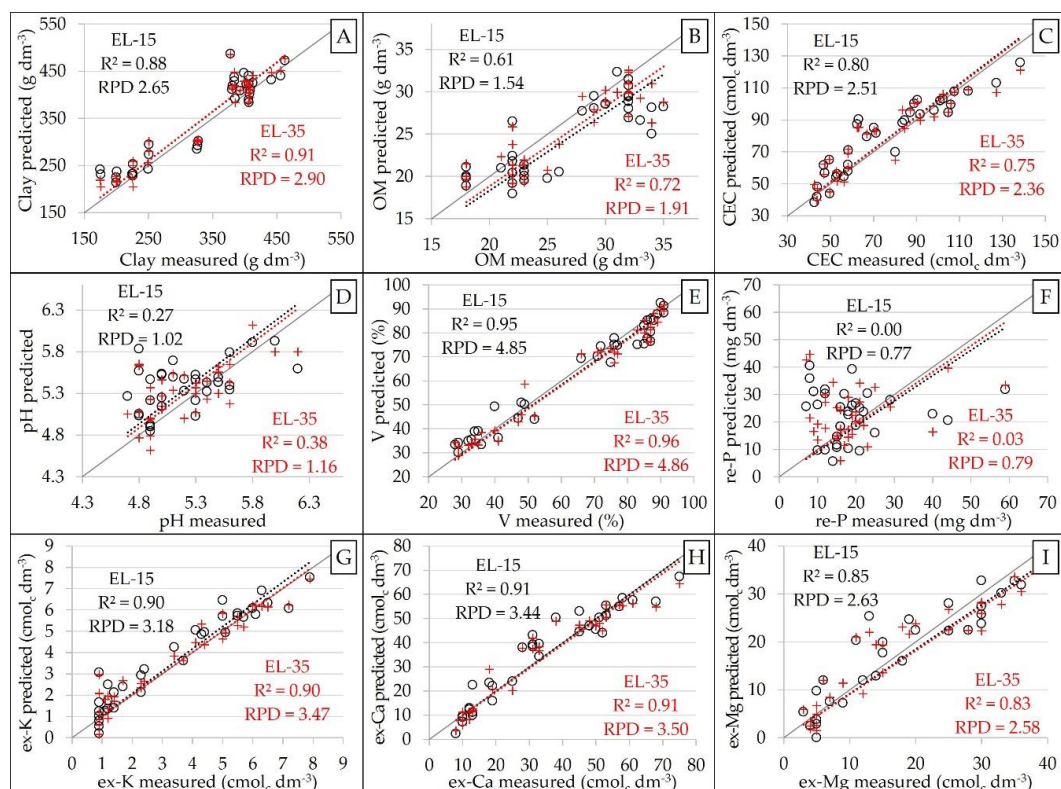


Figure A2. Scatter plots (for the calibration set, $n = 34$) of measured versus predicted clay, organic matter (OM), cation exchange capacity (CEC), pH, base saturation (V), resin-extracted (re-) P, and exchangeable (ex-) K, Ca, and Mg (A–I, respectively), which are predicted using multiple linear regressions (MLR). The data of EL-15 and EL-35 scenarios were represented by circles and crosses, respectively. The coefficient of determination (R^2) and residual prediction deviation (RPD) values are presented in black and red for EL-15 and EL-35 scenarios, respectively.

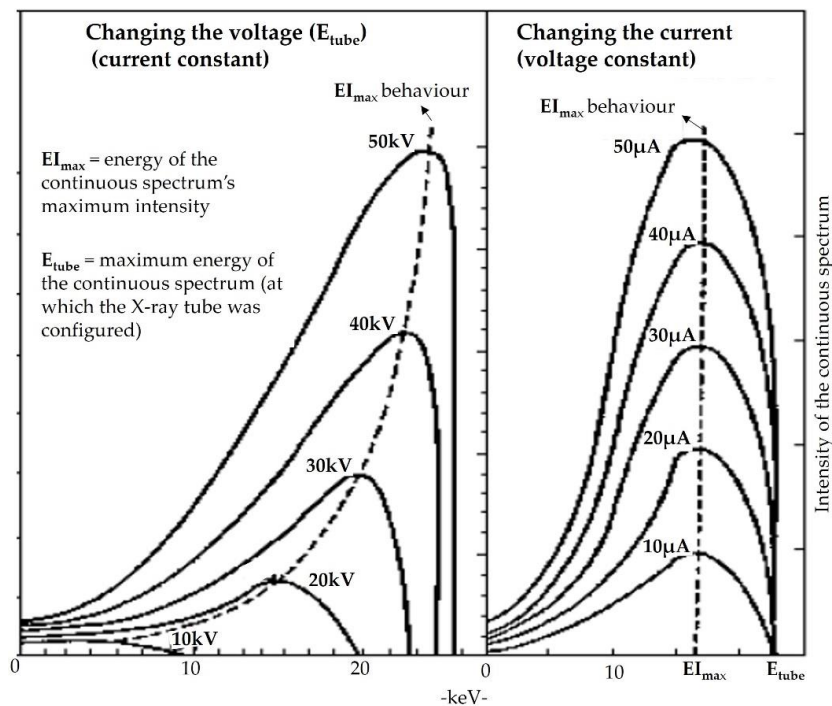


Figure A3. Behavior of the continuous spectrum emitted by the X-ray tube when modifying its voltage (keeping the current constant) and current (keeping the voltage constant) (adapted from Bertin [56]).

Based on Figure A3, and using Equation (A1), as suggested by Taggart Jr et al. [57], the energy of the continuous spectrum's maximum intensity (EI_{\max}) was estimated, in keV, for each X-ray tube configuration.

$$EI_{\max} = E_{\text{tube}}/1.5, \quad (\text{A1})$$

where E_{tube} is the maximum energy, in keV, of the continuous spectrum; in other words, that is the energy corresponding to the voltage that the X-ray tube was configured for. The calculated EI_{\max} was 10.00 and 23.33 keV for the X-ray tube configured at 15 and 35 kV, respectively.

References

1. Molin, J.P.; Tavares, T.R. Sensor systems for mapping soil fertility attributes: Challenges, advances and perspectives in Brazilian tropical soils. *Eng. Agric.* **2019**, *39*, 126–147. [[CrossRef](#)]
2. Viscarra Rossel, R.A.; Bouma, J. Soil sensing: A new paradigm for agriculture. *Agric. Syst.* **2016**, *148*, 71–74. [[CrossRef](#)]
3. Viscarra Rossel, R.; Adamchuk, V.I.; Sudduth, K.A.; McKenzie, N.J.; Lobsey, C. Proximal soil sensing: An effective approach for soil measurements in space and time. *Adv. Agron.* **2011**, *113*, 243–291. [[CrossRef](#)]
4. Kuang, B.; Mahmood, H.S.; Quraishi, M.Z.; Hoogmoed, W.B.; Mouazen, A.M.; van Henten, E.J. Sensing soil properties in the laboratory, in situ, and on-line: A review. *Adv. Agron.* **2012**, *114*, 155–223. [[CrossRef](#)]
5. Nawar, S.; Corstanje, R.; Halcro, G.; Mulla, D.; Mouazen, A.M. Delineation of soil management zones for variable-rate fertilization: A review. *Adv. Agron.* **2017**, *143*, 175–245. [[CrossRef](#)]
6. Ji, W.; Adamchuk, V.I.; Biswas, A.; Dhawale, N.M.; Sudarsan, B.; Zhang, Y.; Rossel, R.A.; Shi, Z. Assessment of soil properties in situ using a prototype portable MIR spectrometer in two agricultural fields. *Biosyst. Eng.* **2016**, *152*, 14–27. [[CrossRef](#)]
7. Archbold, G.; Torres, H.B.; Ruiz, F.; Marín, M.N.; Chaves, D.M.; Arboleda, L.T.; Parra, C.; Carrillo, H.; Mouazen, A.M. pH Measurement IoT System for Precision Agriculture Applications. *IEEE Lat. Am. Trans.* **2019**, *17*, 823–832. [[CrossRef](#)]
8. Weindorf, D.C.; Chakraborty, S.; Herrero, J.; Li, B.; Castañeda, C.; Choudhury, A. Simultaneous assessment of key properties of arid soil by combined PXRF and Vis-NIR data. *Eur. J. Soil Sci.* **2016**, *67*, 173–183. [[CrossRef](#)]

9. Xu, D.; Zhao, R.; Li, S.; Chen, S.; Jiang, Q.; Zhou, L.; Shi, Z. Multi-sensor fusion for the determination of several soil properties in the Yangtze River Delta, China. *Eur. J. Soil Sci.* **2019**, *70*, 162–173. [[CrossRef](#)]
10. Zhang, Y.; Hartemink, A.E. Data fusion of vis–NIR and PXRF spectra to predict soil physical and chemical properties. *Eur. J. Soil Sci.* **2019**. [[CrossRef](#)]
11. Tavares, T.R.; Nunes, L.C.; Alves, E.E.N.; Almeida, E.; Maldaner, L.F.; Krug, F.J.; Carvalho, H.W.P.; Molin, J.P. Simplifying sample preparation for soil fertility analysis by X-ray fluorescence spectrometry. *Sensors* **2019**, *19*, 5066. [[CrossRef](#)]
12. Weindorf, D.C.; Chakraborty, S. Portable X-ray Fluorescence Spectrometry Analysis of Soils. In *Methods of Soil Analysis*; Hirmas, D., Madison, W.I., Eds.; Soil Science Society of America: Wisconsin, WI, USA, 2016; pp. 1–8. [[CrossRef](#)]
13. Zhu, Y.; Weindorf, D.C.; Zhang, W. Characterizing soils using a portable X-ray fluorescence spectrometer: 1. Soil texture. *Geoderma* **2011**, *167*, 167–177. [[CrossRef](#)]
14. Sharma, A.; Weindorf, D.C.; Man, T.; Aldabaa, A.A.A.; Chakraborty, S. Characterizing soils via portable X-ray fluorescence spectrometer: 3, Soil reaction (pH). *Geoderma* **2014**, *232*, 141–147. [[CrossRef](#)]
15. Sharma, A.; Weindorf, D.C.; Wang, D.; Chakraborty, S. Characterizing soils via portable X-ray fluorescence spectrometer: 4, Cation exchange capacity (CEC). *Geoderma* **2015**, *239*, 130–134. [[CrossRef](#)]
16. Rawal, A.; Chakraborty, S.; Li, B.; Lewis, K.; Godoy, M.; Paulette, L.; Weindorf, D.C. Determination of base saturation percentage in agricultural soils via portable X-ray fluorescence spectrometer. *Geoderma* **2019**, *338*, 375–382. [[CrossRef](#)]
17. Nawar, S.; Delbecq, N.; Declercq, Y.; Smedt, P.; Finke, P.; Verdoodt, A.; Meirvenne, M.V.; Mouazen, A.M. Can spectral analyses improve measurement of key soil fertility parameters with X-ray fluorescence spectrometry? *Geoderma* **2019**, *350*, 29–39. [[CrossRef](#)]
18. Towett, E.K.; Shepherd, K.D.; Sila, A.; Aynekulu, E.; Cadisch, G. Mid-infrared and total x-ray fluorescence spectroscopy complementarity for assessment of soil properties. *Soil Sci. Soc. Am. J.* **2015**, *79*, 1375–1385. [[CrossRef](#)]
19. Morona, F.; Santos, F.R.; Brinatti, A.M.; Melquiades, F.L. Quick analysis of organic matter in soil by energy-dispersive X-ray fluorescence and multivariate analysis. *Appl. Radiat. Isotopes* **2017**, *130*, 13–20. [[CrossRef](#)]
20. Silva, S.H.G.; Teixeira, A.F.D.S.; Menezes, M.D.D.; Guilherme, L.R.G.; Moreira, F.M.D.S.; Curi, N. Multiple linear regression and random forest to predict and map soil properties using data from portable X-ray fluorescence spectrometer (pXRF). *Ciênc. Agrotec.* **2017**, *41*, 648–664. [[CrossRef](#)]
21. Andrade, R.; Faria, W.M.; Silva, S.H.G.; Chakraborty, S.; Weindorf, D.C.; Mesquita, L.F.; Guilherme, L.R.G.; Curi, N. Prediction of soil fertility via portable X-ray fluorescence (pXRF) spectrometry and soil texture in the Brazilian Coastal Plains. *Geoderma* **2020**, *357*, 113960. [[CrossRef](#)]
22. Teixeira, A.F.D.S.; Weindorf, D.C.; Silva, S.H.G.; Guilherme, L.R.G.; Curi, N. Portable X-ray fluorescence (pXRF) spectrometry applied to the prediction of chemical attributes in Inceptisols under different land uses. *Ciênc. Agrotec.* **2018**, *42*, 501–512. [[CrossRef](#)]
23. Santos, F.R.; Oliveira, J.F.; Bona, E.; Santos, J.V.F.; Barboza, G.M.; Melquiades, F.L. EDXRF spectral data combined with PLSR to determine some soil fertility indicators. *Microchem. J.* **2020**, *152*, 104275. [[CrossRef](#)]
24. Silva, S.; Poggere, G.; Menezes, M.; Carvalho, G.; Guilherme, L.; Curi, N. Proximal sensing and digital terrain models applied to digital soil mapping and modeling of Brazilian Latosols (Oxisols). *Remote Sens.* **2016**, *8*, 614. [[CrossRef](#)]
25. Silva, E.A.; Weindorf, D.C.; Silva, S.H.; Ribeiro, B.T.; Poggere, G.C.; Carvalho, T.S.; Goncalves, M.G.; Guilherme, L.R.; Curi, N. Advances in Tropical Soil Characterization via Portable X-Ray Fluorescence Spectrometry. *Pedosphere* **2019**, *29*, 468–482. [[CrossRef](#)]
26. Weindorf, D.C.; Zhu, Y.; Mc Daniel, P.; Valerio, M.; Lynn, L.; Michaelson, G.; Clark, M.; Ping, C.L. Characterizing soils via portable x-ray fluorescence spectrometer: 2. Spodic and Albic horizons. *Geoderma* **2012**, *189*, 268–277. [[CrossRef](#)]
27. O'Rourke, S.M.; Stockmann, U.; Holden, N.M.; Mc Bratney, A.B.; Minasny, B. An assessment of model averaging to improve predictive power of portable vis-NIR and XRF for the determination of agronomic soil properties. *Geoderma* **2016**, *279*, 31–44. [[CrossRef](#)]
28. Bowers, C. Matrix Effect Corrections in X-ray Fluorescence Spectrometry. *J. Chem. Educ.* **2019**, *96*, 2597–2599. [[CrossRef](#)]

29. Jenkins, R. *X-Ray Fluorescence Spectrometry*; John Wiley & Sons: Hoboken, NJ, USA, 2012; p. 232.
30. Lindgren, E.S. X-ray fluorescence analysis—energy dispersive. In *Encyclopedia of Analytical Chemistry*; Meyers, R.A., Ed.; John Wiley & Sons: Chichester, UK, 2000; ISBN 0471-97670-9.
31. Potts, P.J.; Webb, P.C.; Watson, J.S. Energy-dispersive x-ray fluorescence analysis of silicate rocks for major and trace elements. *X-Ray Spectrom.* **1984**, *13*, 2–15. [[CrossRef](#)]
32. Panchuk, V.; Yaroshenko, I.; Legin, A.; Semenov, V.; Kirsanov, D. Application of chemometric methods to XRF-data—A tutorial review. *Anal. Chim. Acta* **2018**, *1040*, 19–32. [[CrossRef](#)]
33. IUSS Working Group WRB. World reference base for soil resources 2014. In *World Soil Resources Reports No. 106*; Schad, P., van Huyssteen, C., Micheli, E., Eds.; FAO: Rome, Italy, 2014; p. 189. ISBN 978-92-5-108369-7.
34. Van Raij, B.; Andrade, J.C.; Cantarella, H.; Quaggio, J.A. *Análise Química Para Avaliação de Solos Tropicais*; IAC: Campinas, Brazil, 2001; p. 285. (In Portuguese)
35. Element, C.A.S. Method 3051A microwave assisted acid digestion of sediments, sludges, soils, and oils. *Z. Für Anal. Chem.* **2007**, *111*, 362–366.
36. Silva, Y.J.A.B.; Nascimento, C.W.A.; Biondi, C.M. Comparison of USEPA digestion methods to heavy metals in soil samples. *Environ. Monit. Assess.* **2014**, *186*, 47–53. [[CrossRef](#)] [[PubMed](#)]
37. Currie, L.A. Limits for qualitative detection and quantitative determination. Application to radiochemistry. *Anal. Chem.* **1968**, *40*, 586–593. [[CrossRef](#)]
38. Kennard, R.W.; Stone, L.A. Computer aided design of experiments. *Technometrics* **1969**, *11*, 137–148. [[CrossRef](#)]
39. Chang, C.W.; Laird, D.A.; Mausbach, M.J.; Hurburgh, C.R. Near-infrared reflectance spectroscopy—principal components regression analyses of soil properties. *Soil Sci. Soc. Am. J.* **2001**, *65*, 480–490. [[CrossRef](#)]
40. Stenberg, B.; Viscarra Rossel, R.A.; Mouazen, A.M.; Wetterlind, J. Visible and near infrared spectroscopy in soil science. *Adv. Agron.* **2010**, *107*, 163–215. [[CrossRef](#)]
41. Mouazen, A.M.; De Baerdemaeker, J.; Ramon, H. Effect of wavelength range on the measurement accuracy of some selected soil constituents using visual-near infrared spectroscopy. *J. Near Infrared Spec.* **2006**, *14*, 189–199. [[CrossRef](#)]
42. Van Raij, B. *Fertilidade do Solo e Manejo de Nutrientes*; International Plant Nutrition Institute (IPNI): Piracicaba, São Paulo, Brazil, 2011; p. 420. (In Portuguese)
43. Albertini, V.R.; Paci, B.; Generosi, A. Energy dispersive, X-ray fluorescence analysis. In *Encyclopedia of Analytical Chemistry: Applications, Theory and Instrumentation*; John Wiley & Sons: New York, NY, USA, 2018; pp. 1–17. [[CrossRef](#)]
44. Yılmaz, D.; Boydaş, E. The use of scattering peaks for matrix effect correction in WDXRF analysis. *Radiat. Phys. Chem.* **2018**, *153*, 17–20. [[CrossRef](#)]
45. Lima, T.M.; Weindorf, D.C.; Curi, N.; Guilherme, L.R.; Lana, R.M.; Ribeiro, B.T. Elemental analysis of Cerrado agricultural soils via portable X-ray fluorescence spectrometry: Inferences for soil fertility assessment. *Geoderma* **2019**, *353*, 264–272. [[CrossRef](#)]
46. Schaefer, C.E.G.R.; Fabris, J.D.; Ker, J.C. Minerals in the clay fraction of Brazilian latosols (oxisols): A review. *Clay Miner.* **2008**, *43*, 137–154. [[CrossRef](#)]
47. Singh, B.; Gilkes, R.J. Properties and distribution of iron oxides and their association with minor elements in the soils of south-western Australia. *J. Soil Sci.* **1992**, *43*, 77–98. [[CrossRef](#)]
48. Viscarra Rossel, R.A.; Lobsey, C. *Scoping Review of Proximal Soil Sensors for Grain Growing*; CSIRO: Canberra, Australia, 2016.
49. Fontes, M.P.F. Intemperismo de rochas e minerais. In *Pedologia: Fundamentos*; Ker, J.C., Curi, N., Schaefer, C.E.G.R., Vidal-Torrado, P., Eds.; Sociedade Brasileira de Ciência do Solo: Viçosa, Brazil, 2012; pp. 181–205. (In Portuguese)
50. Hartemink, A.E. Soil science in tropical and temperate regions—Some differences and similarities. *Adv. Agron.* **2002**, *77*, 269–292. [[CrossRef](#)]
51. Oates, K.M.; Kamprath, E.J. Soil acidity and liming: I. Effect of the extracting solution cation and pH on the removal of aluminum from acid soils. *Soil Sci. Soc. Am. J.* **1983**, *47*, 686–689. [[CrossRef](#)]
52. Abreu, C.H., Jr.; Muraoka, T.; Lavorante, A.F. Relationship between acidity and chemical properties of Brazilian soils. *Sci. Agric.* **2003**, *60*, 337–343. [[CrossRef](#)]
53. Pavan, M.A.; Bingham, F.T.; Pratt, P.F. Redistribution of Exchangeable Calcium, Magnesium, and Aluminum Following Lime or Gypsum Applications to a Brazilian Oxisol. *Soil Sci. Soc. Am. J.* **1984**, *48*, 33–38. [[CrossRef](#)]

54. Büchele, D.; Chao, M.; Ostermann, M.; Leenen, M.; Bald, I. Multivariate chemometrics as a key tool for prediction of K and Fe in a diverse German agricultural soil-set using EDXRF. *Sci. Rep.* **2019**, *9*, 1–11. [[CrossRef](#)]
55. Rodrigues, E.S.; Gomes, M.H.F.; Duran, N.M.; Cassanji, J.G.B.; da Cruz, T.N.M.; Sant'Anna Neto, A.; Savassa, S.M.; de Almeida, E.; Carvalho, H.W.P. Laboratory Microprobe X-Ray Fluorescence in Plant Science: Emerging Applications and Case Studies. *Front. Plant Sci.* **2018**, *9*, 1588. [[CrossRef](#)]
56. Bertin, E.P. *Introduction to X-ray Spectrometric Analysis*; Plenum Press: New York, NY, USA, 1978; p. 485.
57. Taggart, J.E., Jr.; Lindsay, J.R.; Scott, B.A.; Vivit, D.V.; Bartel, A.J.; Stewart, K.C. Analysis of geologic materials by wavelength-dispersive X-ray fluorescence spectrometry. In *Methods for Geochemical Analysis*; US Geological Survey Bulletin: Denver, CO, USA, 1987; Volume 1770, pp. E1–E19.



© 2020 by the authors. Licensee MDPI, Basel, Switzerland. This article is an open access article distributed under the terms and conditions of the Creative Commons Attribution (CC BY) license (<http://creativecommons.org/licenses/by/4.0/>).